Xenon plasma Focussed Ion Beam preparation of an Al-6XXX alloy sample for Atom Probe Tomography including analysis of an α-Al(Fe,Mn)Si dispersoid

J.R. Famelton[1], G.M. Hughes[1], C.A. Williams[2], C. Barbatti[3], M.P. Moody[1], and P.A.J. Bagot[1]

[1]Department of Materials, University of Oxford, Oxford, UK
[2]Innoval Technology Ltd, Banbury, UK
[3]Constellium University Technology Centre, Brunel University, London, UK

May 13, 2021

Abstract

A Xe plasma Focussed Ion Beam instrument was used to prepare in-situ specimens for Atom Probe Tomography from a bulk sample of an aluminium 6XXX alloy. The nature and distribution of precipitates and solute clusters observed in the alloy are not observed to differ between standard electropolishing methods and Xe plasma preparation. Enabled by site specific specimen preparation, analysis of an α-Al(Fe,Mn)Si dispersoid shows segregation at the phase boundary and in the shell of the dispersoid.

Keywords; Al-Mg-Si-Cu alloy; Xe plasma focussed ion beam; atom probe tomography; dispersoid.

1 Introduction

Atom Probe Tomography (APT) has been widely used to characterise detailed microstructures in a variety of aluminium alloys [1–7]. A large proportion of the atom probe research currently conducted on aluminium alloys uses specimens prepared by the standard electropolishing method [8]. Electropolishing has several advantages over other specimen preparation methods, in that it is relatively simple and does not require expensive equipment. Many other materials systems prepared for APT are prepared by Focussed Ion Beam (FIB) methods [9, 10], which have the advantage of enabling site specific analysis. Use of conventional Ga based FIBs on aluminium alloys has been limited, due to the high affinity for Ga at grain boundaries [6, 11]. Ga is known to embrittle grain boundaries in aluminium alloys [12] and it is predicted this reduces specimen yield, as discussed by Lilensten and Gault[13]. Furthermore contaminant Ga at a boundary has been observed to alter the boundary chemistry [12]. The presence of excess Ga means the boundary composition is not the same as in the uncontaminated bulk sample, but it can also be that the ratio of the other elements observed at a boundary is not the same as the uncontaminated boundary.

Two possible alternatives to gain the advantages of FIB preparation methods with aluminium alloys have been implemented; cryo-Ga FIB [13], to prevent diffusion of Ga to grain boundaries and a FIB using an alternative ion source [11, 14–16]. Lilensten and Gault [13] prepared a commercial 6016 alloy and observed that holding the sample 90 K or below during milling resulted in a significant decrease in Ga content observed at a grain boundary during APT analysis. An advantage of using an alternative ion source over this approach is that it removes any doubt that Ga observed in the specimen is intrinsic or extrinsic to the specimen. The use of a Xe plasma FIB (PFIB) with aluminium alloy samples and applying the commonly used lift-out method [17] has been demonstrated [11, 14–16] and has been successful at isolating grain boundaries without Ga contamination.

These works do not assess whether other damage mechanisms due to the Xe beam are occurring. Estivill et al. [18] observed small clusters of Xe atoms in Si APT specimens produced with a Xe PFIB, which they suggested were due to the formation of nano-scale Xe bubbles in the specimen during milling. It was also observed that crystallinity was lost in the surface 50 nm of Si. Such features have not been reported in the Al specimens, although these studies[11, 15, 16] all applied a final 5 kV or lower polishing step to remove FIB damaged material. A few nm thick amorphous layer was observed via Transmission Electron Microscopy in a Ti alloy by Halpin et al. [19] who applied a 2 kV polish.

Halpin et al. also showed that due to the higher beam current often achievable with a Xe-PFIB [20] a different procedure of tip production is possible. By milling a circular trench into the surface of a bulk sample they completely removed the need for a lift-out step onto a Si micro-post coupon and a weld region in the final specimen, as used in the standard method

[17]. A universal, albeit empirical, observation amongst APT researchers is specimen fracture at the weld between Si micro-post and sample, therefore eliminating this feature could improve yield of successful analyses for certain materials. In this work, the use of a Xe-PFIB for aluminium specimen production without lift-out will be demonstrated and the results compared with a conventional electropolished specimen.

It will then be shown how this approach has also enabled analysis of a dispersoid precipitate, isolated and captured within an APT specimen via this specimen preparation route. Dispersoid precipitates are formed during homogenisation of Al alloys and often occur heterogeneously [21, 22]. Identification and extraction of these types of features is logistically problematic if relying upon electropolishing specimen preparation methods and successful APT analysis is made significantly more likely using FIB methods.

2 Experimental procedure

An extruded Al-Mg-Si-Cu alloy was examined in this study. The alloy was received in as extruded form from Constellium and subsequently had a short pre-age treatment applied. The nominal alloy composition is Al - 0.6 Mg - 0.6 Si - 0.3 Cu at % with total other additions less than 0.2 at%. APT specimens were prepared via two routes. Standard two stage electropolishing techniques [23, 24] were used to produce needle specimens using first a solution of 15 % perchloric acid, 10 % water and 75 % acetic acid by volume and followed by a solution of 1.2 % perchloric acid, 0.8 % water and 98 % 2-butoxyethanol by volume. Voltages in the range 20 V to 10 V were used, with lower voltages used as the needle became thinner.

Xe-PFIB work was carried out using a ThermoFisher Helios$^{\mathrm{TM}}$ G4 PFIB CXe. Samples were prepared by standard metallographic preparation techniques of polishing with diamond suspension and colloidal silica. The polished samples were then attached to a Cu holder by using a silver suspension (silver DAG 1415M) and transferred to the PFIB in a specially adapted pin stub, as shown in Fig. 1a. The procedure described by Halpin et al. [19] was adapted and is shown in Fig. 1b-e.

The milling procedure can be split into two steps; the circular trench mill and sharpening. The “tab” milled for laser access to the specimen by Halpin et al[19] was found to be unnecessary. Coarse milling was performed to remove the bulk of the material from around the region of interest. This process was scripted using iFast (ThermoFisher software) to generate sets of concentric annuli with a constant inner radius, but decreasing outer radius. This has the effect of producing a stepped base of the milled circular trench, with a pillar of material remaining in the centre. The first set of patterns were milled over an annulus of outer/inner radii 150/20 μm using 30 kV/2.5 μA milling conditions. A further mill was carried out, with milling conditions of 30 kV/60 nA, using a second set of concentric annuli with a set of reduced outer radii (Fig. 1d). This setup reduced the milling time considerably over the perpendicular edged trench (single annulus) technique (Fig. 1c)[19]. Differing milling rates depending on grain orientation led to a rougher base to the trench (Fig. 1c-d) than the specimens produced by Halpin et al. [19], however this was not found to be an issue for APT experiments.

The sharpening stage of milling, Fig. 1d-e, was not automated and used standard annular milling techniques, with a range of annuli sizes and milling currents. A final low voltage polishing step was applied to remove the material most damaged by the Xe beam, using 5 kV/1 nA milling conditions and removing at least 300 nm of material, as monitored by the electron beam. In order to determine the effects of ion beam induced damage and artefacts on the surface material, some specimens were prepared without this final polishing step. The entire process, from selecting a region on the sample surface, to finished specimen, takes around two hours, the first half of which is the automated circular trench mill.

Once milling was complete the Cu holder was removed from the pin stub and transferred to a Cameca LEAP^{TM} 5000 XR. All APT datasets shown here were collected using laser pulsing, with laser pulse energy of 100 pJ. The specimens were held at a stage temperature of 50 K and a pulse rate of 125 kHz was used. APT datasets were reconstructed using the Cameca IVAS^{TM} visualisation software. Calibration of reconstruction parameters was carried out using the methodology described by Gault et al. [25]. Overlaps of peaks with the same or similar mass-to-charge state ratio was carried out using custom MATLAB code, as described by London [26][27] and was used for compositional line profiles. Solute cluster identification was performed using the open source software Posgen [28], using the maximum separation method [29]. Values of cluster defining parameters d_{max} and N_{min} were selected based on the methodology of Williams et al. [30], and were in the range of 0.75 - 0.85 nm for d_{max} and 16 - 23 atoms of Mg, Si and/or Cu for N_{min}.

3 Results and Discussion

3.1 Assessment of PFIB induced damage

Xe implantation into the surface of the specimen is observable in the APT reconstruction of the specimen prepared without a 5 kV polishing step (Fig.

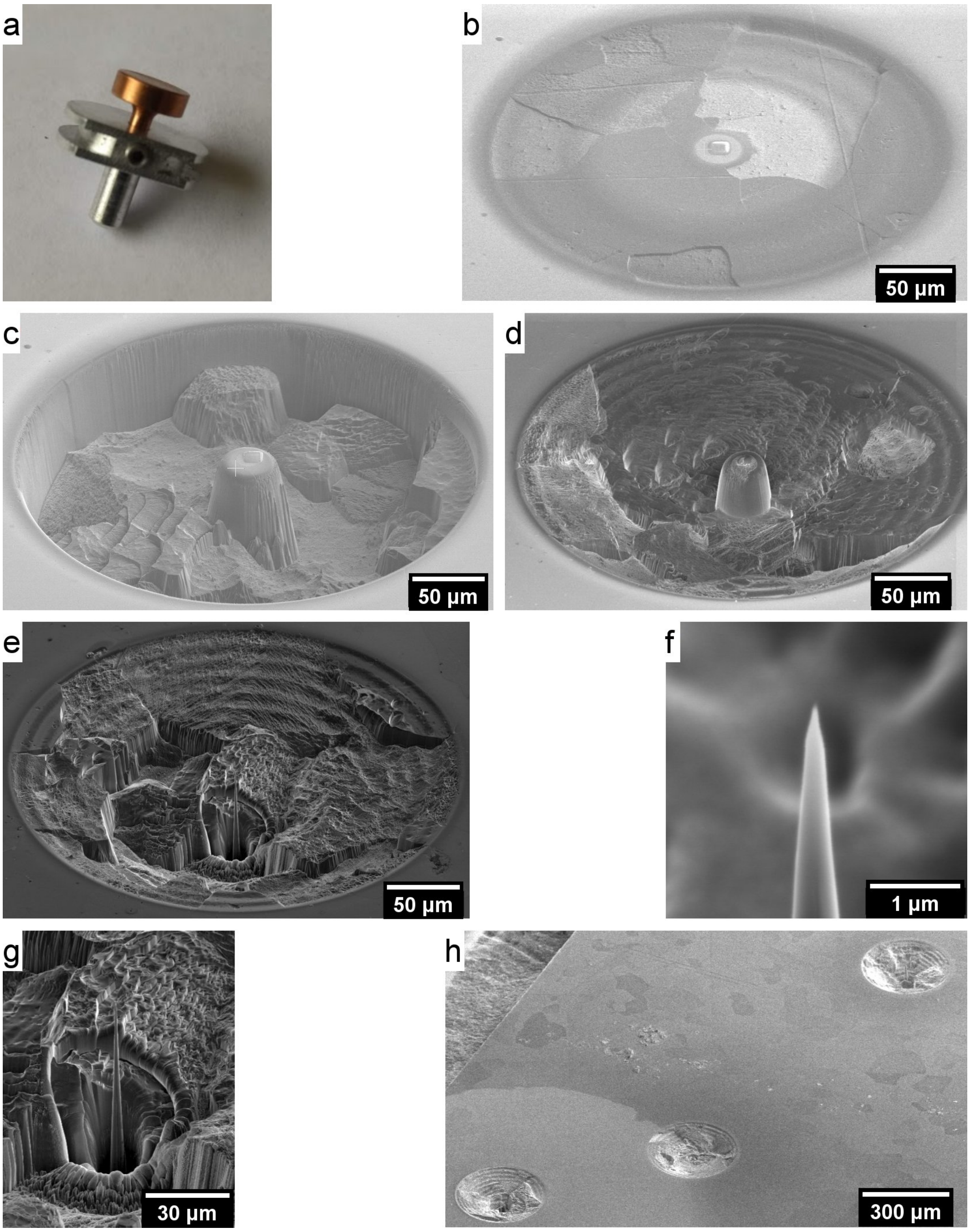

Figure 1: Images of the sample preparation process. a) Sample mount b) Start of automated milling, after protective platinum layer has been deposited on the sample surface c) Perpendicular edge trench d) Stepped edge trench e) Fully prepared specimen f) High magnification image of tip after 5 kV polish g) Centre of milled region h) Overview of bulk sample surface showing multiple specimens milled into the same surface.

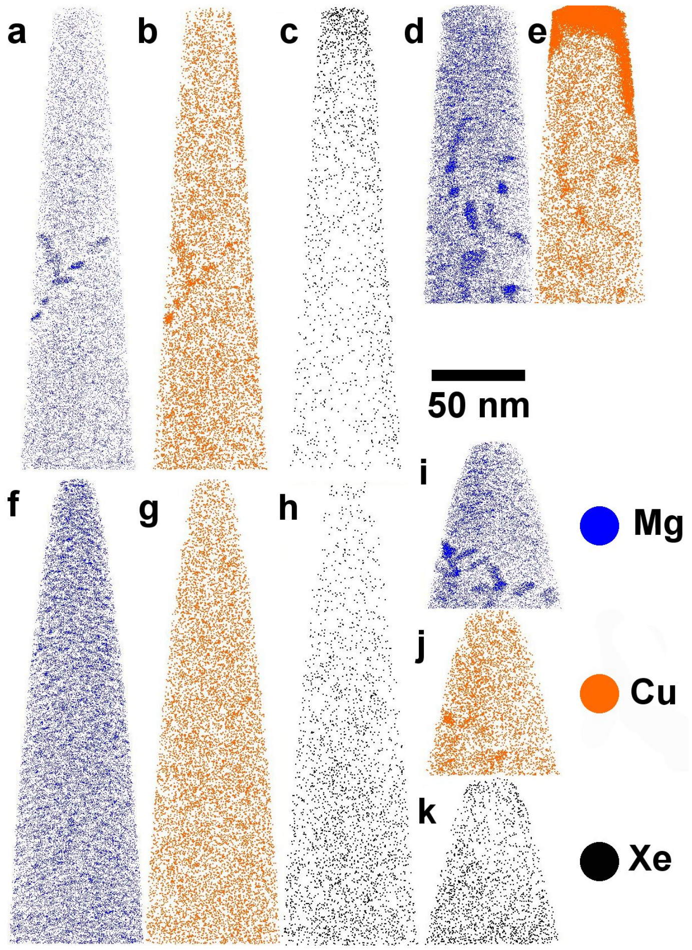

Figure 2: Al - 6XXX selected atom maps. 20 nm thick slices from atom maps showing Mg, Cu and Xe. a)-c) PFIB no polish d)-e) Electropolished f)-h) PFIB 5 kV polish A i)-k) PFIB 5 kV polish B

2c). In the specimens which did receive the polishing step, no peaks in the whole dataset mass spectrum due to Xe were detected, as shown for one of these such samples in Fig. 3b. Ranging the relevant regions in the mass spectrum there is also no obvious Xe segregation apparent in the atom maps (Fig. 2h and k). However, by extracting the first 20 nm of this dataset, were it might be expected to find any implanted Xe, peaks due to the presence of Xe^+ ions are observed (Fig. 3c). Due to the small number of Xe ions detected, the composition of Xe needs to be assessed with comparison to the local background counts, which can change throughout an APT dataset [31].

Figure 4 shows line profiles of the concentration of Xe as a function of depth from the apex of the APT reconstruction. Local background correction

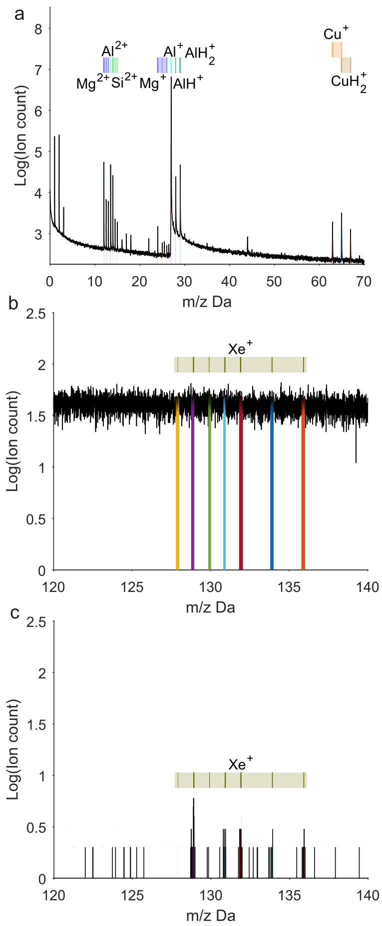

Figure 3: a; Mass spectrum of PFIB 5 kV polish C, typical of all the mass spectra, with major peaks labelled. Bands above the spectrum indicate the positions of the expected peaks for a given ion. Thickness of the lines within the bands indicate the relative sizes of peaks expected based on natural isotopic abundances. b; Section of mass spectrum of whole PFIB 5kV polish C dataset, showing the range of mass-to-charge ratios which would encompass Xe^+ ions. c; Same section of mass spectrum as in b but only for ions from the apex 20 nm of the dataset. Peaks due to Xe^+ ions are visible above background noise

has been made by fitting an exponential function to the portion of the mass spectrum at a lower mass-to-charge ratio than the ranged window. The error bars shown indicate one standard deviation in this background correction. Using this method low levels of Xe are observed in the first 50 nm of material when a polishing step has been carried out. Beyond 50 nm the amount of

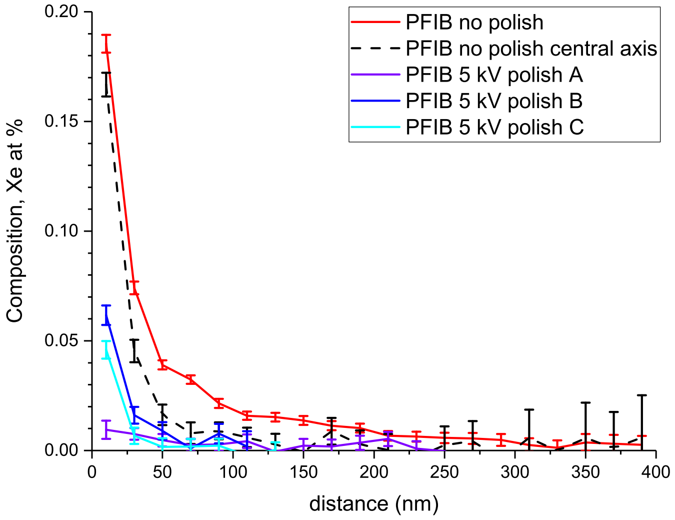

Figure 4: one dimensional concentration profile for Xe as a function of distance from specimen apex. Local background correction has been applied and error bars are 1 standard deviation of the applied background correction

Xe is below the detection limit. Higher concentrations of implanted Xe are left in the specimen generated in the absence of a final 5 kV polishing step. Two profiles are provided for this specimen, one is for the whole dataset and shows there is Xe present in the specimen upto 300 nm for the specimen apex. The other profile shows the Xe composition of a 15 nm radius cylinder along the central axis of the specimen. There is Xe present to a depth of 100 nm along the central axis. The Xe is implanted to a depth of upto 100 nm into the surface, but can be found at the surface of the sample at a greater depth due to the needle shaped nature of the specimen.

In comparison, electropolishing is known to potentially cause contamination of Cu on the surface of an APT specimen [32], as was observed here (Fig. 2e), there is a surface layer of Cu deposited during the electropolishing process. This layer is particularly problematic for the analysis of this family of alloys, as the segregation of Cu is of interest to solute cluster and precipitation behaviour [33]. Excess Cu ions detected can affect the measured matrix and cluster compositions and the potential identification of solute clusters. The presence of Cu contamination means that relatively large sections of data need to be discarded and long datasets with sufficient regions fully free of the Cu contamination are required, to obtain a representative analysis.

There is variation of Mg content between specimens that is greater than the confidence interval for the different datasets. In particular the specimen PFIB 5 kV polish A contains more Mg than the other specimens with the same treatment. APT samples small volumes of material and some variation between samples is expected. The PFIB specimens have similar bulk compositions and composition profiles to the electropolished specimen. There is also no effect on the solute content in the regions were Xe implantation was observed. Notably however the surface Cu and oxygen content of the electropolished specimen is much higher. Oxide formed on the surface of the specimen during electropolishing may be thicker than the native oxide formed on the specimens after FIB milling. The Xe clusters observed in the Si specimens of Estivill et al.[18], which were produced solely with a 30 kV accelerating voltage, were not observed.

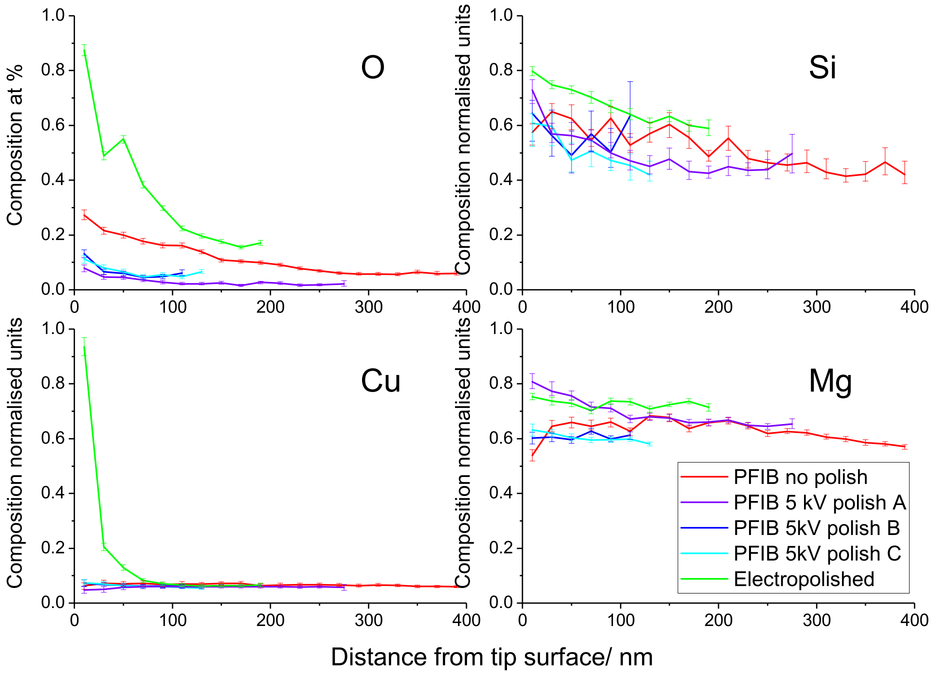

Figure 5: One dimensional concentration profiles of O, Si, Cu and Mg as a function of distance from specimen apex. Error bars indicate a 95% confidence interval in the solving of mass-to-charge state overlaps by maximum likelihood estimation as described by London [26]. For each of the elements Si, Cu and Mg the 5 line profiles have been normalised by the same factor such that the scale is from zero to 1 dimensionless units.

3.2 Solute distribution

Heterogeneous precipitates, thought to be nucleating on dislocations, have been observed in all three specimen preparation conditions. It is therefore unlikely the FIB milling process is creating damage that is leading to nucleation of such precipitates. The precipitates here are defined to be features which contain over 200 detected solute atoms (Mg, Si and Cu) although there is also solute segregation involving fewer atoms. Solute clustering is more likely to be affected by the heat input during milling as the diffusion distances involved are shorter and the solute clusters are believed to be less thermally stable [34]. The size distribution of solute clusters and precipitates observed is shown in Fig. 6. The clusters sizes observed do not vary significantly between the electropolished and PFIB prepared specimens, other than the electropolished specimen contains a higher proportion of larger features. This specimen is however a smaller dataset, which contains a heterogeneous feature, which will skew the distribution. Far more solute clusters were analysed using PFIB preparation due to the larger volume of data analysed. The 1365 clusters found in the PFIB prepared specimens were richer in Mg than Si containing on average, 53 ± 10 at% Mg, 38 ± 9 at% Si and 8 ± 5 at% Cu. The 67 clusters found in the electropolished specimen have a very similar composition containing on average 57 ± 11 at% Mg, 33 ± 11 at% Si and 9 ± 6 at% Cu. The precipitates observed also all have a similar ternary composition between specimen preparation methods (Fig. 6d). There is a narrower observed composition range of Cu and a wider range of Mg:Si ratios.

3.3 α-Al(Fe,Mn)Si dispersoid

Figure 7a-f shows a dispersoid precipitate observed in the same alloy and heat treatment condition as the other specimens shown. The dispersoid is partially contained within the dataset, so that two perpendicular sides of the dispersoid are observed. The ionic species shown in the atom maps show that the dipersoid itself is rich in Si and Fe and that Mg and Cu are segregated to the phase boundary between the matrix and dispersoid. There are also precipitates which contain Mg, Si and Cu in the Al matrix region surrounding the dispersoid. One precipitate was observed at the phase boundary between Al matrix and the dispersoid (Fig. 7b).

In order to show the full elemental segregation between the aluminium matrix and dispersoid a proximity histogram [35] was generated, showing composition as a function of distance from the interface (Fig. 8). The interface was defined by an iso-concentration surface of 8 at% Si^{2+} ions. This species was used to define the interface as its mass-to-charge state ratio does

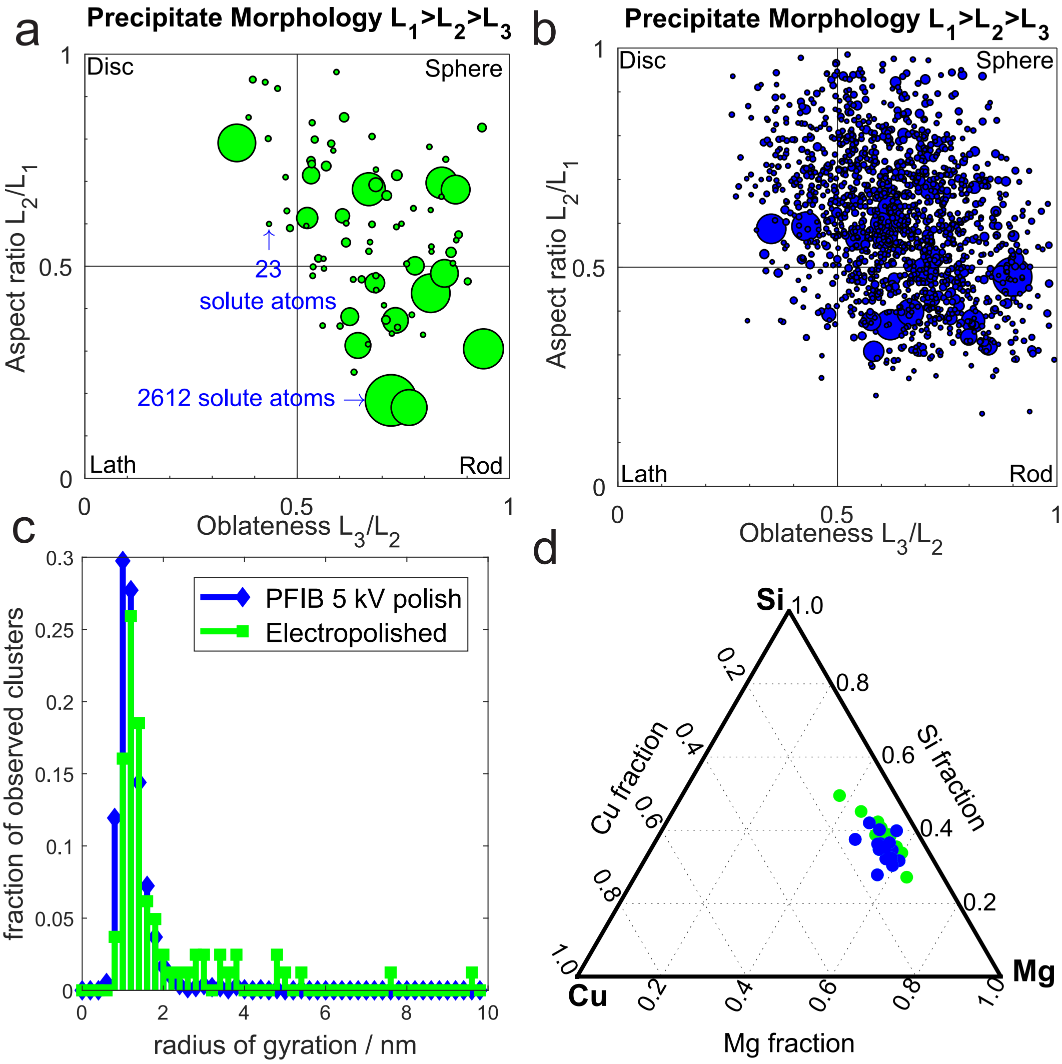

Figure 6: a) and b) Plots of aspect ratio against oblateness for a) PFIB 5 kV polished specimens and b) An electropolished specimen. Spot area is proportional to number of solute atoms detected. c) Normalised histograms of solute cluster and precipitate radii of gyration. d) Ternary compositions of the observed precipitates (over 200 detected solute atoms).

not overlap with any other species present in this specimen. 8 at% was used as at this value the surface intersected closely with the thin Mg layer observed in Fig. 7g. The section of the interface containing the phase boundary precipitate was excluded from this analysis. To generate the proximity histogram ions were separated into bins of width 2 nm, radiating outwards from the interface. For each bin the overlaps of mass-to-charge state ratio

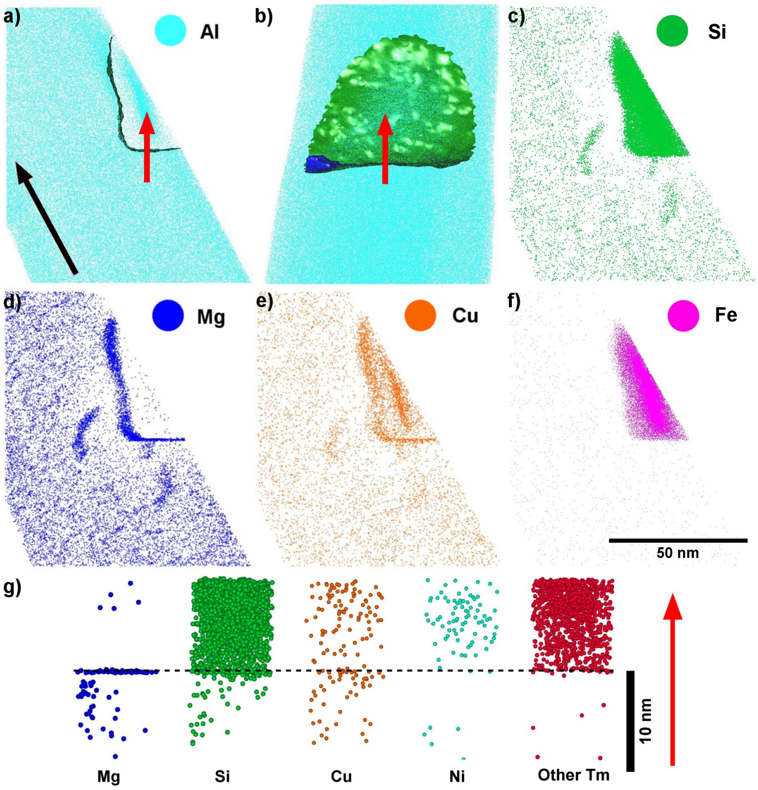

Figure 7: Atom maps in the region of an α-Al(Fe,Mn)Si dispersoid. a) 20 nm thick slice showing Al and a surface showing 8 at% concentration of Si^{2+} (green). The black arrow indicates orientation of specimen central axis. b) 90°rotation of region shown in a). A surface showing 17 at% Mg^{2+} (blue) indicating a phase boundary precipitate is also shown. c)-f) 20 nm thick slices showing the same region as a) for selected elements. c) Si. d) Mg. e) Cu. f) Fe. g) Cylinder of diameter 8 nm taken from the region indicated by the red arrow in a) and b) showing Mg, Si, Cu, Ni and other transition metals (Mn, Cr and V) from left to right. The dashed line indicates the same plane in the 5 atom maps.

were solved using the method of London[26]. The important species which overlap in this material are; Al^{+}, Si^{+} and Fe^{2+} and associated XH_n hydride ions. A local consideration of mass-to-charge state overlaps is required in this case as the relative ratios of these species is expected to change between the two phases.

From the proximity histogram, Fig. 8, segregation within the Al matrix and the dispersoid can be observed. Both phases can be split into two regions. The matrix has a very low amount of transition metal species, apart

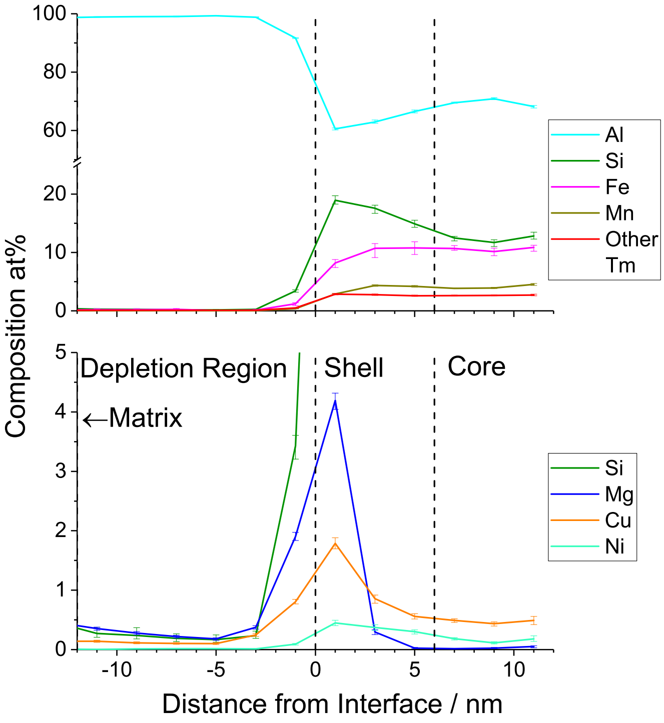

Figure 8: Proximity histogram showing composition as a function of distance from the interface defined by 8 at% Si^{2+} and shown in Fig. 7a-b. Four regions and their approximate distance from the this interface are identified; Matrix < -10 nm; -10 nm < Depletion Region < 0 nm; 0 nm < Dispersoid Shell < 6 nm; Dispersoid Core > 6 nm. The error bars indicate a 95% confidence interval in the solving of mass-to-charge state overlaps by maximum likelihood estimation as described by London [26]

from Cu. Within approximately 10 nm of the interface the concentration of the elements which form the strengthening precipitates, Mg, Si and Cu, is decreased. The precipitates found around the dispersoid mainly occur around the boundary between the bulk matrix and depletion region, with one precipitate forming at the interface and one in the depletion region. It is thought that precipitates in the matrix have nucleated on dislocations around the dispersoid. The effect of dispersoids on the distribution of strengthening precipitate forming solute and heterogeneous nucleation of precipitates is important for understanding the role that they play on the overall mechanical properties of the alloy [36, 37].

The dispersoid exhibits a core-shell structure. The core of the dispersoid is richer in Al compared to the shell, which is enriched in Si and Ni. The other transition metals present, Fe, Mn, Cr and V show no preference for the shell or core. The proximity histogram allows for the solving of mass-to-charge overlaps which requires sufficient ionic counts to be accurate. This is at the expense however of spatial resolution. A one dimensional concentration profile though the highest spatial resolution section of the interface has been produced to give a more detailed profile of the spatial segregation.

Figure 7g shows an 8 nm diameter cylindrical section, extracted normal to the boundary from the region indicated by the red arrow in fig7a and b. This cylinder is nearly parallel to the local surface normal of the hemispherical surface on which the reconstruction is based, and is thus the section of the phase boundary which has the greatest spatial resolution [38]. A one dimensional concentration profile was generated from this region of the phase boundary, using a bin width of 0.05 nm, and is shown in Figure9. The zero point of this profile is defined by the peak in the Mg concentration. From this profile it can be determined that Mg and Cu are segregating to the phase boundary between the matrix and dispersoid. The peaks in concentration of these two elements occur at the same position at which the elements that form the dispersoid, such as Si and Mn increase. The Ni enrichment occurs away from the boundary in the shell of the dispersoid. The Cu is less strongly segregated to the phase boundary than Mg. Cu is also detected within the dispersoid, while Mg is only present in the matrix and at the phase boundary.

Figure 9 shows the density of ions overlaid with the concentration of Mg. This is the density of ranged ions in the dataset, with no correction made for the absence of ions due to detector efficiency. The region next the boundary on the dispersoid side of the boundary is lower in density. This leads to the shell width appearing wider in the reconstruction. This distortion in the reconstruction is caused by the differing evaporation fields of the two phases [39, 40]. Based on the number of ions in the shell region, we estimate the shell thickness to be approximately 1 to 4 nm thick (1 to 3 dispersoid units

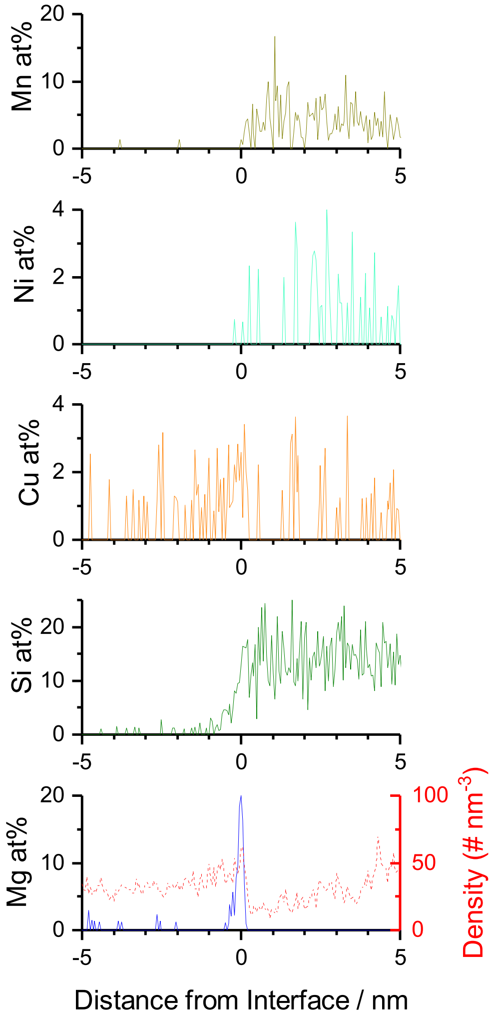

Figure 9: One dimensional concentration profiles from the region shown in fig7g. No mass-to-charge overlap solving has been done due to the small volume size. For each element shown only some isotopes and charge states have been included to avoid major mass to charge overlaps. This provides a more accurate measurement of the relative positions of the these elements, however compositional measurements should not be relied on. Elements shown from top to bottom, with m/z values of the relevant peaks indicated in brackets, are; Mn (27.5 55), Ni(58 60 62), Cu (63 65 67(CuH_2^+)), Si (14, 14.5 15) and Mg (12, 12.5, 13, 24). The origin of the distance from interface is defined by the peak in the Mg concentration profile. The density of ions as a function of distance from the interface is overlaid with the Mg concentration profile.

cells).

Multiple types of dispersoid precipitate are possible, however in this type of alloy it is expected that α-Al(Mn,Fe)Si dispersoids form. The equilibrium structure and composition of this phase has been calculated [41–43]. Multiple works have observed variations in Mn/Fe ratio in this structure [44, 45] and inclusion of Cr [21, 46]. The proposed unit cell contains 138 atoms, with 11 distinct lattice environments. Three of these lattice environments, making up 30 of the 138 atoms in a unit cell, have mixed occupancy of Al and Si [43]. This leads to the equilibrium composition of $\mathrm{Al_{69.7}Mn_{17.4}Si_{12.9}}$, however if all potential Si sites were occupied by Si the composition would be $\mathrm{Al_{60.9}Mn_{17.4}Si_{21.7}}$. This literature value and theoretical value are compared to the observed composition of the dispersoid in Fig. 10. The transition metals which showed no segregation to the shell or core are combined; Fe, Mn, Cr and V. The solute elements which were present in the dispersoid, but showed segregation to the phase boundary and/or shell are combined also for comparison; Si, Cu and Ni. The core composition agrees well with the expected composition from Sugiyama et al. [43], especially if the small amounts of Cu and Ni are considered to occupy the same lattice sites as Si in the structure. In the shell, the concentration of these segregated species increases towards, but does not exceed, the theoretical maximum Si content.

The authors are only aware of one work which has observed core-shell segregation in an α-Al(Mn,Fe)Si type dispersoid [46]. Flament et al. observed Cr segregation to the shell of an α-Al(Mn,Fe,Cr)Si dispersoid, which was not observed in this case. They were unable to measure the distribution of Al and Si via electron energy loss spectroscopy. The alloy chemistry and thermal history however are not the same which could potentially account for the difference in observation. It should be noted that it is the late period transition metals, Ni and Cu which show preference for the shell or phase boundary while the earlier period transition metals Fe, Mn, Cr and V do not.

4 Conclusions

The use of a Xe-PFIB for preparation of aluminium APT specimens without lift-out has been demonstrated. Using similar low accelerating voltage polishing steps as used with standard Ga FIB specimen preparation methods, specimens can be produced with minimal artefacts due to the Xe beam. Despite the relative ease with which elements diffuse in aluminium alloys at room temperature, no change in solute distribution was detectable. Xe-PFIB is a useful technique for aluminium APT specimen production, allowing effective site specific analysis. The milling procedure used is simple and quick

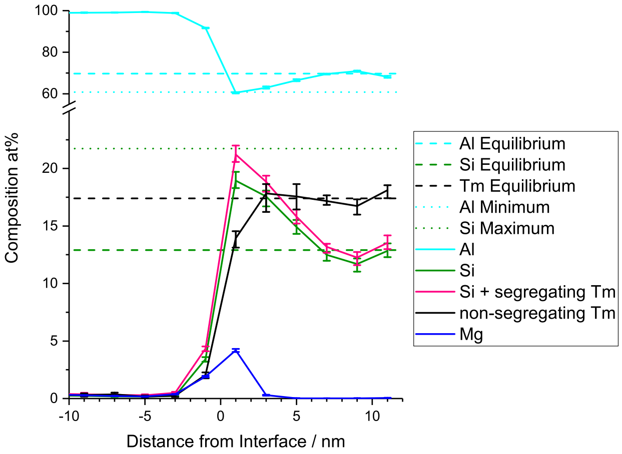

Figure 10: Compositional profile from Fig. 8 with selected elements combined. Horizontal dashed lines indicate the expected compositions based on the structural work of Sugiyama et al. [43].

compared to lift-out specimen preparation methods, with fewer critical steps. As well as reducing the time taken to prepare samples, the ability to automate the circular trench mill reduces the required user input.

Using this specimen preparation technique, the complex chemical structure around an α-Al(Fe,Mn)Si dispersoid was analysed, providing detailed chemical and spatial information unachievable via other methods. Mg and Cu were observed to segregate to the Al and dispersoid phase boundary. A core-shell structure was also observed, with Si and trace amounts of some transition metals thought to replace Al in the shell of the dispersoid, while elements thought to sit on transition metal sites show no core/shell preference.

5 Acknowledgements

The authors would like to thank Constellium for financially supporting this research and providing the materials. The authors are grateful to the UK Engineering and Physical Science Research Council (EPSRC) for funding of the LEAP 5000XR for the UK National Atom Probe Facility through grant EP/M022803/1.

The authors acknowledge use of characterisation facilities within the David Cockayne Centre for Electron Microscopy, Department of Materials, University of Oxford. The authors would also like to acknowledge the financial support of the Henry Royce Institute (through EPSRC grant EP/R010145/1) for capital equipment and financial support.

6 Data Availability

The raw/process data required to reproduce these findings cannot be shared at this time as the data also forms part of an ongoing study.

References

[1] P. Dumitraschkewitz, S. S. A. Gerstl, L. T. Stephenson, P. J. Uggowitzer, and S. Pogatscher. Clustering in Age-Hardenable Aluminum Alloys. *Advanced Engineering Materials* 20.10 (Oct. 2018), 1800255. DOI: `10.1002/adem.201800255`.

[2] K. E. Knipling, R. A. Karnesky, C. P. Lee, D. C. Dunand, and D. N. Seidman. Precipitation evolution in Al-0.1Sc, Al-0.1Zr and Al-0.1Sc-0.1Zr (at.%) alloys during isochronal aging. *Acta Materialia* 58.15 (Sept. 2010), 5184–5195. DOI: `10.1016/j.actamat.2010.05.054`.

[3] M. Timpel, N. Wanderka, R. Schlesiger, T. Yamamoto, N. Lazarev, D. Isheim, G. Schmitz, S. Matsumura, and J. Banhart. The role of strontium in modifying aluminium-silicon alloys. *Acta Materialia* 60.9 (May 2012), 3920–3928. DOI: `10.1016/j.actamat.2012.03.031`.

[4] A. Biswas, D. J. Siegel, C. Wolverton, and D. N. Seidman. Precipitates in Al-Cu alloys revisited: Atom-probe tomographic experiments and first-principles calculations of compositional evolution and interfacial segregation. *Acta Materialia* 59.15 (Sept. 2011), 6187–6204. DOI: `10.1016/j.actamat.2011.06.036`.

[5] V. Araullo-Peters, B. Gault, F. D. Geuser, A. Deschamps, and J. M. Cairney. Microstructural evolution during ageing of Al-Cu-Li-x alloys. *Acta Materialia* 66 (Mar. 2014), 199–208. DOI: `10.1016/j.actamat.2013.12.001`.

[6] F. Tang, D. Gianola, M. P. Moody, K. Hemker, and J. Cairney. Observations of grain boundary impurities in nanocrystalline Al and their influence on microstructural stability and mechanical behaviour. *Acta Materialia* 60.3 (Feb. 2012), 1038–1047. DOI: `10.1016/J.ACTAMAT.2011.10.061`.

[7] G. Sha, H. Möller, W. E. Stumpf, J. H. Xia, G. Govender, and S. P. Ringer. Solute nanostructures and their strengthening effects in Al-7Si-0.6Mg alloy F357. *Acta Materialia* 60.2 (2012), 692–701. DOI: `10.1016/j.actamat.2011.10.029`.

[8] A. K. Ceguerra and R. K. Marceau. Atom Probe Tomography of Aluminium Alloys: A Systematic Meta-Analysis Review of 2018. *Metals* 9.10 (Oct. 2019), 1071. DOI: `10.3390/met9101071`.

[9] M. Miller, K. Russell, and G. Thompson. Strategies for fabricating atom probe specimens with a dual beam FIB. *Ultramicroscopy* 102.4 (Mar. 2005), 287–298. DOI: `10.1016/J.ULTRAMIC.2004.10.011`.

[10] T. F. Kelly and D. J. Larson. The second revolution in atom probe tomography. *MRS Bulletin* 37 (2012), 150–158. DOI: `10.1557/mrs.2012.3`.

[11] B. Gault, A. J. Breen, Y. Chang, J. He, E. A. Jägle, P. Kontis, P. Kürnsteiner, A. Kwiatkowski Da Silva, S. K. Makineni, I. Mouton, Z. Peng, D. Ponge, T. Schwarz, L. T. Stephenson, A. Szczepaniak, H. Zhao, and D. Raabe. Interfaces and defect composition at the near-atomic scale through atom probe tomography investigations. *Journal of Materials Research* 33.23 (Dec. 2018), 4018–4030. DOI: `10.1557/jmr.2018.375`.

[12] J. Y. Uan and C. C. Chang. Gallium-induced magnesium enrichment on grain boundary and the gallium effect on degradation of tensile properties of aluminum alloys. *Metallurgical and Materials Transactions A: Physical Metallurgy and Materials Science* 37.7 (July 2006), 2133–2145. DOI: `10.1007/BF02586134`.

[13] L. Lilensten and B. Gault. New approach for FIB-preparation of atom probe specimens for aluminum alloys. *PLOS ONE* 15.4 (Apr. 2020). Ed. by H. R. Bakhsheshi-Rad, e0231179. DOI: `10.1371/journal.pone.0231179`.

[14] K. Fisher and E. Marquis. "Comparing Plasma-FIB and Ga-FIB Preparation of Atom Probe Tomography Samples". *Microscopy and Microanalysis*. Vol. 22. S3. Cambridge University Press (CUP), July 2016, 692–693. DOI: `10.1017/s1431927616004311`.

[15] H. Zhao, F. De Geuser, A. Kwiatkowski da Silva, A. Szczepaniak, B. Gault, D. Ponge, and D. Raabe. Segregation assisted grain boundary precipitation in a model Al-Zn-Mg-Cu alloy. *Acta Materialia* 156 (Sept. 2018), 318–329. DOI: `10.1016/j.actamat.2018.07.003`.

[16] H. Zhao, Y. Chen, B. Gault, S. K. Makineni, D. Ponge, and D. Raabe. (Al, Zn)3Zr dispersoids assisted η' precipitation in anAl-Zn-Mg-Cu-Zr alloy. *Materialia* 10 (May 2020), 100641. DOI: `10.1016/j.mtla.2020.100641`.

[17] D. W. Saxey, J. M. Cairney, D. McGrouther, T. Honma, and S. P. Ringer. Atom probe specimen fabrication methods using a dual FIB/SEM. *Ultramicroscopy* 107.9 (Sept. 2007), 756–760. DOI: `10.1016/j.ultramic.2007.02.024`.

[18] R. Estivill, G. Audoit, J. P. Barnes, A. Grenier, and D. Blavette. Preparation and Analysis of Atom Probe Tips by Xenon Focused Ion Beam Milling. *Microscopy and Microanalysis* 22.3 (Feb. 2016), 576–582. DOI: `10.1017/S1431927616000581`.

[19] J. E. Halpin, R. W. Webster, H. Gardner, M. P. Moody, P. A. Bagot, and D. A. MacLaren. An in-situ approach for preparing atom probe tomography specimens by xenon plasma-focussed ion beam. *Ultramicroscopy* 202 (July 2019), 121–127. DOI: `10.1016/j.ultramic.2019.04.005`.

[20] M. M. V. Taklo, A. Klumpp, P. Ramm, L. Kwakman, and G. Franz. Bonding and TSV in 3D IC Integration: Physical Analysis with a Plasma FIB. *Microscopy and Analysis* 25.7 (2011), 9–12.

[21] L. Lodgaard and N. Ryum. Precipitation of dispersoids containing Mn and/or Cr in Al–Mg–Si alloys. *Materials Science and Engineering: A* 283.1-2 (May 2000), 144–152. DOI: `10.1016/S0921-5093(00)00734-6`.

[22] F. Qian, S. Jin, G. Sha, and Y. Li. Enhanced dispersoid precipitation and dispersion strengthening in an Al alloy by microalloying with Cd. *Acta Materialia* 157 (Sept. 2018), 114–125. DOI: `10.1016/j.actamat.2018.07.001`.

[23] M. Miller, A. Cerezo, M. G. Hetherington, and G. Smith. *Atom Probe Field Ion Microscopy.* Oxford University Press, 1996.

[24] B. Gault, M. P. Moody, J. M. Cairney, and S. P. Ringer. *Atom Probe Microscopy.* Vol. 160. Springer Series in Materials Science. New York, NY: Springer New York, 2012. DOI: `10.1007/978-1-4614-3436-8`.

[25] B. Gault, M. P. Moody, F. De Geuser, G. Tsafnat, A. La Fontaine, L. T. Stephenson, D. Haley, and S. P. Ringer. Advances in the calibration of atom probe tomographic reconstruction. *Journal of Applied Physics* 105.3 (Feb. 2009), 034913. DOI: `10.1063/1.3068197`.

[26] A. J. London. Quantifying Uncertainty from Mass-Peak Overlaps in Atom Probe Microscopy. *Microscopy and Microanalysis* 25.2 (Apr. 2019), 378–388. DOI: `10.1017/S1431927618016276`.

[27] A. J. London. *Atomprobelab v2.2.* https://sourceforge.net/projects/atomprobelab/ Accessed 30/03/20, 2020.

[28] D. Haley. *Posgen 0.0.3.* https://apttools.sourceforge.io/ Accessed 28/04/20, 2017.

[29] J. M. Hyde and C. A. English. "An Analysis of the Structure of Irradiation induced Cu-enriched Clusters in Low and High Nickel Welds". *MRS Proceedings.* Vol. 650. Cambridge University Press, Mar. 2000, R6.6. DOI: `10.1557/PROC-650-R6.6`.

[30] C. A. Williams, D. Haley, E. A. Marquis, G. D. Smith, and M. P. Moody. Defining clusters in APT reconstructions of ODS steels. *Ultramicroscopy* 132 (Sept. 2013), 271–278. DOI: `10.1016/j.ultramic.2012.12.011`.

[31] D. Larson, T. Prosa, R. Ulfig, B. Geiser, and T. Kelly. *Local electrode atom probe tomography.* 1st ed. Springer, 2013. DOI: `DOI10.1007/978-1-4614-8721-0`.

[32] D. Haley, I. McCarrol, P. A. J. Bagot, J. M. Cairney, and M. P. Moody. A gas-phase reaction cell for modern Atom Probe systems. *Microscopy and Microanalysis* 25.2 (Jan. 2019), 410–417. DOI: `10.1017/S1431927618016240`. arXiv: `1901.05883`.

[33] S. Wenner, C. D. Marioara, S. J. Andersen, and R. Holmestad. Effect of room temperature storage time on precipitation in Al–Mg–Si(–Cu) alloys with different Mg/Si ratios. *International Journal of Materials Research* 103.8 (Aug. 2012), 948–954. DOI: `10.3139/146.110795`.

[34] M. Werinos, H. Antrekowitsch, T. Ebner, R. Prillhofer, P. Uggowitzer, and S. Pogatscher. Hardening of Al–Mg–Si alloys: Effect of trace elements and prolonged natural aging. *Materials & Design* 107 (Oct. 2016), 257–268. DOI: `10.1016/j.matdes.2016.06.014`.

[35] O. C. Hellman, J. A. Vandenbroucke, J. Rüsing, D. Isheim, and D. N. Seidman. Analysis of three-dimensional atom-probe data by the proximity histogram. *Microscopy and Microanalysis* 6.5 (Jan. 2000), 437–444. DOI: `10.1007/s100050010051`.

[36] Z. An, W. Yang, H. Zhan, B. Hu, Q. Wang, S. Matsumura, and G. Sha. On the strengthening effect of Al-Cr-Si dispersoid in an Al-Si-Mg-Cu casting alloy with Cr addition. *Materials Characterization* 166 (Aug. 2020), 110457. DOI: `10.1016/j.matchar.2020.110457`.

[37] K. Strobel, M. A. Easton, M. D. H. Lay, P. A. Rometsch, S. Zhu, L. Sweet, N. C. Parson, and A. J. Hill. Quench Sensitivity in a Dispersoid-Containing Al-Mg-Si Alloy. *Metallurgical and Materials Transactions A: Physical Metallurgy and Materials Science* 50.4 (Apr. 2019), 1957–1969. DOI: `10.1007/s11661-019-05130-2`.

[38] B. Gault, M. P. Moody, F. De Geuser, A. La Fontaine, L. T. Stephenson, D. Haley, and S. P. Ringer. Spatial Resolution in Atom Probe Tomography. *Microscopy and Microanalysis* 16.1 (Feb. 2010), 99–110. DOI: `10.1017/S1431927609991267`.

[39] F. Vurpillot, A. Bostel, and D. Blavette. Trajectory overlaps and local magnification in three-dimensional atom probe. *Applied Physics Letters* 76.21 (May 2000), 3127–3129. DOI: `10.1063/1.126545`.

[40] C. Fletcher, M. P. Moody, and D. Haley. Fast modelling of field evaporation in atom probe tomography using level set methods. *Journal of Physics D: Applied Physics* 52.43 (Oct. 2019), 435305. DOI: `10.1088/1361-6463/ab3703`.

[41] M. Cooper and K. Robinson. The crystal structure of the ternary alloy α(AlMnSi). *Acta Crystallographica* 20.5 (May 1966), 614–617. DOI: `10.1107/S0365110X6600149X`.

[42] M. Cooper. The crystal structure of the ternary alloy α(AlFeSi). *Acta Crystallographica* 23.6 (Dec. 1967), 1106–1107. DOI: `10.1107/S0365110X67004372`.

[43] K. Sugiyama, N. Kaji, and K. Hiraga. Re-refinement of α-(AlMnSi). *Acta Crystallographica Section C: Crystal Structure Communications* 54.4 (Apr. 1998), 445–447. DOI: `10.1107/S0108270197015989`.

[44] P. Donnadieu, G. Lapasset, B. Thanaboonsombut, and T. H. Sanders. "Alpha-phase particles in 6XXX aluminum alloys". *The 4th international conference on aluminum alloys.* 1994, 668–675.

[45] C. L. Liu, Q. Du, N. C. Parson, and W. J. Poole. The interaction between Mn and Fe on the precipitation of Mn/Fe dispersoids in Al-Mg-Si-Mn-Fe alloys. *Scripta Materialia* 152 (July 2018), 59–63. DOI: `10.1016/j.scriptamat.2018.04.012`.

[46] C. Flament, J. Ribis, J. Garnier, T. Vandenberghe, J. Henry, and A. Deschamps. Electron irradiation-enhanced core/shell organization of Al(Cr, Fe, Mn)Si dispersoids in Al–Mg–Si alloys. *Philosophical Magazine* 95.8 (Mar. 2015), 906–917. DOI: `10.1080/14786435.2015.1009959`.

A Appendix Peak assignments and mass-to-charge overlaps

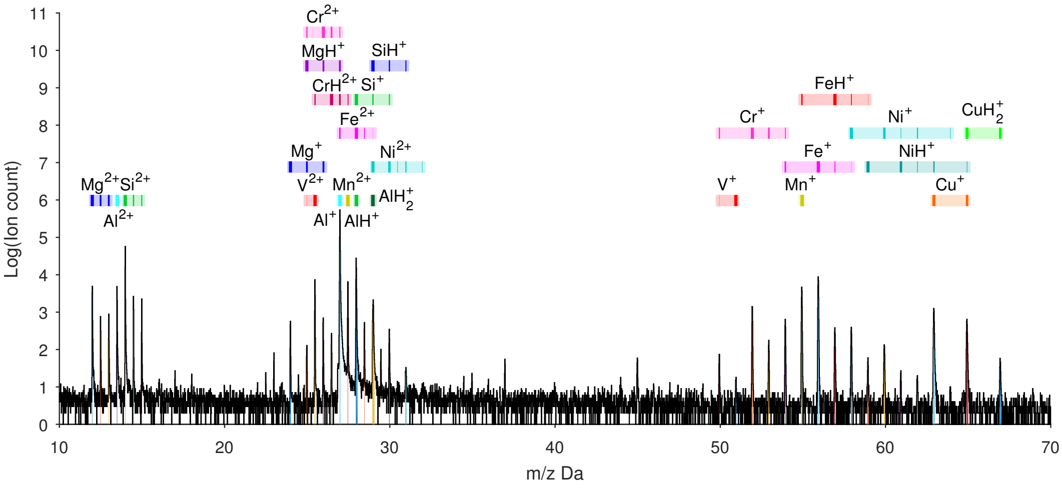

Figure A.1: Mass spectrum of whole dispersoid and part of the surrounding matrix. The major ions are labelled. The coloured horizontal bars indicate the range of mass-to-charge ratios over which a species could be observed. The thickness of vertical lines within the bar indicate the relative abundance of each peak expected for natural isotopic ratios.

The dispersoid precipitate shown in the main body of this work contains several elements which have mass-to-charge ratios which are within 0.1 da. This section describes how some of these overlap problems were dealt with.

Figure A.1 shows the mass spectrum for the whole dispersoid precipitate and part of the surrounding matrix. The main overlaps occur around the 24 - 30 da region and 50 -70 da region. Here we focus on the 24-30 da region as it is more complex. The overlaps in the 50-70 da region were solved using the maximum likelihood approach described by [26], considering the ions displayed in figure A.1. The 24-30 da region contains peaks due to light elements in single charge state and heavier transition metals in a 2+ charge state.

The main complexity comes from the overlapping of AlH^+, $AlH_2{}^+$, Si^+, SiH^+, Fe^{2+} and Ni^{2+}. If all these ions are considered for the mass-to-charge overlap solving there in insufficient information to fully solve this problem [26]. However as we will we show conclusions can still be drawn about the composition and distribution of these ions in the APT dataset. The composition profiles of selected ranges across the dispersoid interface are shown in

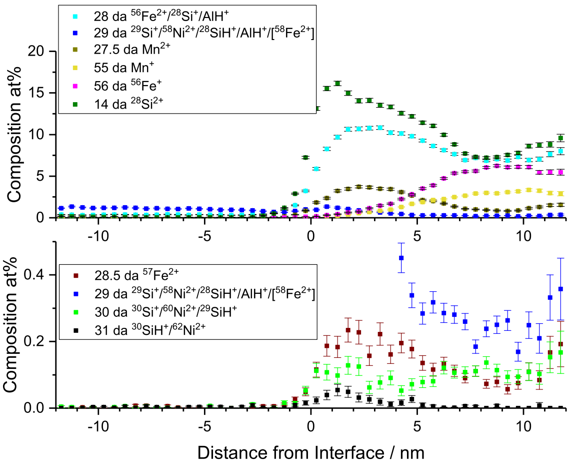

Figure A.2: Composition profile of selected ranges across the dispersoid interface. The surface used is the same as in the main body of work; isoconcentration surface of 8 at % Si^{2+}. Error bars indicate 1 standard deviation in the estimation of the background correction to each range.

figure A.2. The potential identities of ions contained within each range are given in the figure key. Mn has no major mass-to-charge overlaps in either the 1+ or 2+ charge state. The composition of Mn^{2+} is greater around the interface and shell of the dispersoid, while there is more Mn^{+} in the core of the dispersoid. The combination of these charge states leads to a uniform composition within the dispersoid as shown in the main body of the work. A similar distribution of the two charge states is observed for other non-overlapping or weakly overlapping ions, such as Al, Cr, and V. This effect is thought to be due to a locally higher electric field during evaporation.

The non-overlapping $^{57}Fe^{2+}$ species also has a greater composition around the interface and shell, while the $^{56}Fe^{+}$ ions are found more in the core. Based on the $^{57}Fe^{2+}$ composition, the total composition of Fe^{2+} from all isotopes can be estimated, as well as the contribution to individual ranges. Si^{2+} is segregated to the interface and shell of the precipitate, similarly to other 2+ charge state ions. In this case though the degree of is Si segregation to the shell is such that there are not enough ions which could be Si^{+} to even out the segregation, as was observed for other elements, such as Fe, Mn, Cr and V.

The 28 da peak is thought to be a combination of the ions, $^{56}Fe^{2+}$, $^{28}Si^{+}$ and AlH^{+}. A large proportion of ions ranged in this peak are found in the dispersoid and are due to $^{56}Fe^{2+}$, as estimated by the $^{57}Fe^{2+}$ peak. These three ions have slightly different mass-to-charge ratios. It can be seen in the mass spectrum that there is a double peak due to the difference in mass. Although the peaks from the three ions partially overlap, by ranging the different sections of the peak it can observed if the different ions are found preferentially in different sections of the dataset. Figure A.3 shows how the 28 da and 29 da peaks have been split into multiple ranges, and the compositional profiles of these ranges across the dispersoid interface are shown in figure A.4. For 28 da the lower mass side of the peak has very low composition in the matrix and is concentrated more in the shell of the dispersoid than the core. The higher mass section of the peak is segregated to the matrix, peaks slightly around the interface and then drops in the dispersoid core. The middle section also increases in composition around the dispersoid interface, but unlike the other parts of the peak, increases in composition in the dispersoid core. This increase in composition towards the core is thought to be due to $^{28}Si^+$. The same analysis applied to the 29 da peak, shows that the higher mass part of the peak, primarily expected to be due to $AlH_2{}^+$, is segregated to the matrix and drops to almost zero composition in the dispersoid core, with no peak at the interface. The lower mass side of the peak meanwhile peaks around the dispersoid interface and has a non-zero composition in the dispersoid.

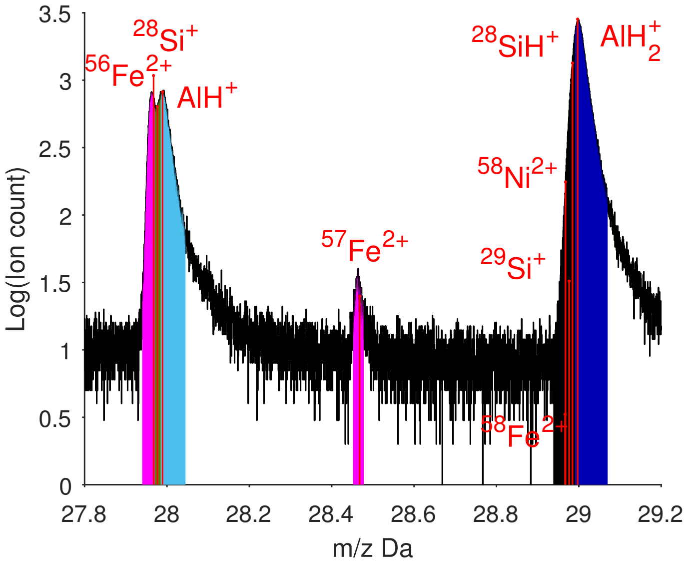

Figure A.3: Section of mass spectrum form figure A.1. Red lines indicate the expected mass-to-charge ratio for the ions that potentially lead to these peaks in the mass spectrum. The shaded sections as the spectrum indicate the ranges used to produce the composition profiles in figure A.4.

The lower mass section of the peak could be due to; $^{29}Si^+$, which is

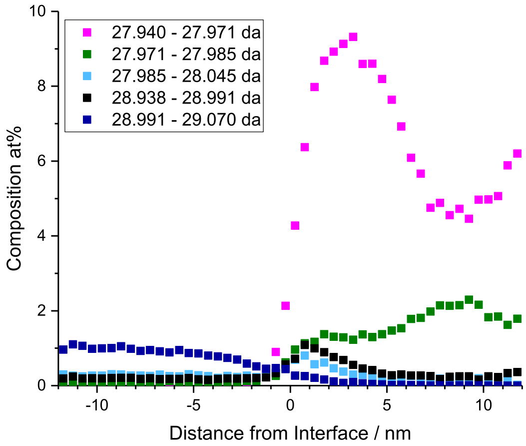

Figure A.4: Composition profiles of selected ranges across the dispersoid interface. The surface from which the profile is generated and the total ranged area of the mass spectrum are the same as in figure A.2.

expected to be segregated more to the dispersoid core, based on the split ranging of the 28 da peak; $^{28}\mathrm{SiH}^{+}$; $^{58}\mathrm{Ni}^{2+}$ or combination of these ions.

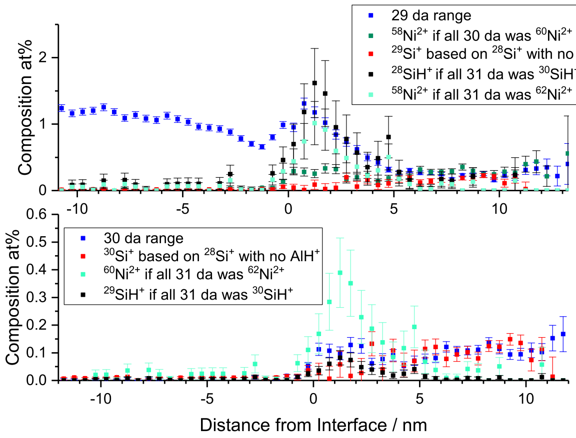

Figure A.5: Top Panel: Composition profile of the 29 da range across the dispersoid interface and the estimated composition profiles of several ions which could contribute the 29 da peak. Bottom Panel: The same profile and estimated contributions for the 30 da range. Error bars indicate 1 standard deviation in the estimation of the background correction to each range.

For each of these possible three ions an estimation of how much they could contribute to the 29 da peak was made, based on other peaks which contain that species. The maximum potential $^{29}\mathrm{Si}^{+}$ contribution was determined by scaling the amount of $^{28}\mathrm{Si}^{+}$ present at 28 da, if there was no AlH^{+} and the amount of $^{56}\mathrm{Fe}^{2+}$ was in the expected isotopic ratio with $^{57}\mathrm{Fe}^{2+}$. The maximum $^{58}\mathrm{Ni}^{2+}$ content was estimated by using the next two most abundant isotopes and assuming they made up all the counts within the ranges they would be found. The same procedure was applied for $^{28}\mathrm{SiH}^{+}$ based on there being a maximum amount of $^{30}\mathrm{SiH}^{+}$in the 31 da range. Based on the 31 da peak the contribution to 29 da could be $^{28}\mathrm{SiH}^{+}$ or $^{58}\mathrm{Ni}^{2+}$. However applying the same maximum content approach to the 30 da range shows that not enough $^{60}\mathrm{Ni}^{2+}$ is observed for it to be the main contributor to the peak in 29 da. The observed composition of the 29 da, 30 da and 31 da ranges in the dispersoid can be explained by the overlap of Si^{+} and SiH^{+}. There is no conclusive evidence that there is Ni^{2+} observed in the spectrum. For this reason Ni^{2+} was left out of the maximum likelihood mass-to-charge overlap solving [26] implemented in the main body of this work. The other ions considered in this overlap region are shown in figure A.1, not including Ni^{2+}.

Any Ni^{2+} that there is present makes up a small proportion of the dispersoid and is expected to be observed more in the shell of the dispersoid, based on the charge state behaviour of the other ions present. It is observed that the ranges which contain a majority Ni^{+} contribution are segregated to the shell which suggests there is Ni segregation to the shell as this charge state is expected more in the core than the shell.